

# Gradual Magnetic Evolution of Sunspot Structure and Filament-Corona Dynamics Associated with the X1.8 Flare in AR 11283

GUIPING RUAN<sup>1</sup>, YAO CHEN<sup>1</sup>, and HAIMIN WANG<sup>2,3</sup>

1 Shandong Provincial Key Laboratory of Optical Astronomy and Solar-Terrestrial  
Environment, and Institute of Space Sciences, Shandong University, Weihai 264209, China;

yaochen@sdu.edu.cn

2 Space Weather Research Laboratory, Center for Solar-Terrestrial Research, NJIT,  
Newark, NJ07102, USA

3 Big Bear Solar Observatory, 40386 North Shore, Big Bear City, CA 92314, USA

Received \_\_\_\_\_; accepted \_\_\_\_\_

## ABSTRACT

In this paper, we present a study on persistent and gradual penumbral decay and correlated decline of the photospheric transverse field component during 10-20 hours before a major flare (X1.8) eruption on 2011 September 7. This long-term pre-eruption behavior is corroborated with the well-imaged pre-flare filament rising, the consistent expansion of coronal arcades overlying the filament, as well as the NLFFF modelling results in the literature. We suggest that both the long-term pre-flare penumbral decay and the transverse field decline are the photospheric manifestation of the gradual rise of the coronal filament-flux rope system. We also suggest that a C3 flare and subsequent reconnection process preceding the X1.8 flare play an important role in triggering the later major eruption.

*Subject headings:* Sun: coronal mass ejections (CMEs) — Sun: flares — Sun: photosphere — Sun: filaments, prominences

## 1. Introduction

Photospheric and corona magnetic field evolution is essential to the energy build-up and release process of solar eruptions. The field evolution is closely related to changes of sunspot structures. It is thus of vital importance to establish the physical connection between the photospheric magnetic field, the sunspot evolution, and the coronal dynamics.

Many previous studies have been focusing on flare-induced changes of the photospheric magnetic field and sunspot structures (e.g., Severny 1964; Wang et al., 1994; Spirock et al., 2002; Yurchyshyn et al., 2004; Wang & Liu 2010; Wang et al., 2012; Liu et al., 2014). Over the past five decades with growing observational capabilities, it was established that the sunspot structure and corresponding photospheric magnetic field may change suddenly and irreversibly after flares. The flare-induced changes are manifested in the rapid change of the transverse photospheric magnetic field ( $B_h$ ), and darkening as well as decay or even disappearance of sunspot structures.

In a recent study, Liu et al. (2014) presented a comprehensive comparison of two major events released from the same NOAA active region (AR 11283). Both events are characterized by X-class flares (an X2.1 one on 2011 September 6 and an X1.8 one on September 7), with fast filament eruptions and coronal mass ejections (CMEs). The authors found that both flares result in rapid increases of  $B_h$  around the flaring polarity inversion line (PIL) and decreases in the surrounding peripheral penumbral region, corresponding to the darkening or decay in white-light (WL) intensities respectively. This is interpreted as the result of the inward collapse of the central magnetic field (also see Hudson, 2000) and the radial outward stretching of the peripheral magnetic field during the flare-CME eruption.

From the space weather forecasting perspective, it is more important to figure out whether there exist some general trends in the pre-flare photospheric magnetic field and

WL evolutions of involved sunspots. In Ruan et al. (2014), a study focusing on the 6-hour long pre-flare sunspot activities and photospheric magnetic field evolution of the X2.1 event from AR 11283 was presented. It was concluded that the persistent sunspot rotation plays an important role in twisting, energizing, and destabilizing the coronal filament-flux rope system. During the period of apparent sunspot rotation, it was found that both horizontal field strength ( $B_h$ ) and the inclination angle ( $\theta_B$  the angle between the vector magnetic field and the local radial direction) decline gradually. They found that the variation of the surface field and the inclination angle is associated with the overall ascending motion of the corona filament-flux rope structure.

Ruan et al. (2014) proposed that the long-term pre-flare evolution of the photospheric  $B_h$  can be taken as a possible precursor of an eruption. In addition, the photospheric field evolution carries information about the energy storage and triggering process of the event, and can be used to discern different eruption mechanism. It was suggested that a gradual decrease of  $B_h$  may be a precursor for an eruption in terms of the flux rope instability (see, e.g., Lin et al., 2003), while a persistent increase of this quantity may be a precursor of the tether-cutting reconnection scenario (Moore 2001).

In this study, we investigate the X1.8 flare on 2011 September 7, occurred in the same AR as studied by Ruan et al. (2014). As mentioned, this event was associated with a fast CME-filament eruption, very similar to the preceding X2.1 event according to the Solar Dynamics Observatory (SDO; Pesnell et al., 2012) data. Our focus is the long-term pre-flare evolution of the photospheric magnetic field and the sunspot structure, and their correlation with the pre-eruption dynamics in the upper layers of the solar atmosphere.

## 2. Observations and the overall profile of the event

For this study, we mainly analyzed the multi-wavelength imaging data provided by the Atmospheric Imaging Assembly (AIA; Lemen et al. 2012) and the vector magnetic field and continuum intensity data by the Helioseismic and Magnetic Imager (HMI; Schou et al. 2012) on board the Solar Dynamic Observatory (SDO). The AIA data at passbands of 304 Å (HeII,  $T \sim 0.05$  MK), 171 Å (FeIX,  $\sim 0.6$  MK) and the 94 Å (FeXVIII,  $T \sim 6.3$  MK) are examined in order to reveal the filament and coronal dynamics at different temperatures. The processed disambiguated HMI vector magnetic field data are of 12-minute cadence at a  $0.5''$  pixel resolution, provided by the HMI team (see <ftp://pail.stanford.edu/pub/HMIvector2/movie/ar1283.mov> for the movie). We also used the HMI continuum intensity observation at the 6173 Å to investigate the evolution of the sunspot structure. These intensity data have been normalized and removed of limb darkening effect with a cadence of 12 minutes and a  $0.5''$  pixel resolution. We also examined the TiO image (a proxy for continuum at 7057 Å) taken by the New Solar Telescope (NST; Goode et al. 2010; Cao et al. 2010) at Big Bear Solar Observatory (BBSO) with a high spatial resolution of about  $0.04''/\text{pixel}$ .

The AR 11283 was located N14W30 at 19:55 UT on September 7, close to the disk center. As mentioned, it released two X-class flares on September 6 and 7, respectively. The eruption processes of both events have been well-studied by many authors (Feng et al., 2013; Jiang et al., 2013; Wang et al., 2012; Zharkov et al., 2013; Ruan et al., 2014; Liu et al. 2014; Shen et al. 2014). So details of the overall evolution of this AR will not be repeated here.

In Figure 1, we show the GOES SXR (1-8 Å) light curve from 20:00 UT Sept. 6 to 24:00 UT Sept. 7. The X1.8 flare started at 22:32 UT, peaked at 22:38 UT, and ended at 22:44 UT according to the GOES data. A C3 flare took place from 19:55 UT to 20:19 UT

with a peaking time at 20:06 UT, which is also of interest to this study. The peaking times of these three flares have been labeled with blue vertical dotted lines. According to the CDAW (Coordinated Data Analysis Workshops) catalog of the LASCO data (Brueckner et al. 1995), the X1.8 flare was accompanied by a CME travelling at a linear speed of  $792 \text{ km s}^{-1}$ .

In Figure 2, we present overall structure of this active region at several observing wavelengths. Panel (a) is the BBSO high-resolution image taken at 18:15 UT to show details of the sunspot structure. The image has been rotated by  $-22.6^\circ$  to facilitate comparison with the SDO data. Panel (b) is for the HMI 6173 Å intensity data in a similar field of view (FOV) as that of panel (a). Panel (c) is taken from the HMI vector magnetic field data of this AR with the color map representing the vertical field component ( $B_z$ ) and arrows for the  $B_h$  component. Panels (d) to (f) present the 304, 171, and 94 Å images recorded by SDO around the same time. The contours are given by  $\pm 300 \text{ G}$  of the HMI vertical field component ( $B_z$ ) on the solar surface. This figure shows some pre-eruption condition of the AR.

The large-scale magnetic field is quadrupolar, with the two spots on the west giving a  $\delta$  configuration, in which the negative one being the leading and the positive one being the following spot. Both X-class flares occurred in similar areas in this AR (Liu et al., 2014). The yellow line in panel (c) delineates an "L"-shaped PIL. The HMI movie given above provides the long-term evolution of the sunspot and the magnetic field, from which we observe that the following  $\delta$  spot continues to move eastward after the X2.1 flare (peaking at 22:20 UT, September 6). The magnetic field around the PIL is almost parallel to the PIL indicating a severely-sheared state of the magnetic field. This is consistent with the transverse alignment of the surrounding filamentary penumbral structures as seen in panel (a) of Figure 2.

Liu et al. (2014) measured the shearing speed of the two opposite-polarity spots in this  $\delta$  configuration, and detected a weaker converging motion along the north-south direction. In addition, after a careful inspection of the HMI data, we find some signatures of rotation of the positive  $\delta$  spot, although no clear features like a well-developed magnetic tongue can be used to undoubtedly trace the rotation (see, e.g., Ruan et al., 2014). No apparent flux emergence is observed during the period between the X2.1 and the X1.8 flare. Generally speaking, the above existing sunspot motions continuously transport energy to the corona through their magnetic connection, and play a fundamental role in pushing the corona state to the eruptive point.

The 304-171-94 Å images presented in panels (d)-(f) and the accompanying animation show the pre-eruption structures and dynamics of the filament and the corona. We can see the filament is above the PIL with the northern foot rooted in the positive spot umbra. It has a sigmoidal shape, corresponding to the hot sigmoidal structure observed with 94 Å. The filament-sigmoid structure has often been taken as the signature of a twisted flux rope structure (e.g., Rust & Kumar 1994; Titov & Demoulin 1999; McKenzie & Canfield 2008), which shall carry a major part of the free magnetic energy to be released.

Now let us inspect the dynamic evolution of the relevant filament-corona structure. Initially, the filament is buried underneath the overlying coronal arcades (171 Å). As the region evolves, the coronal arcades expand gradually and continuously, especially those arcades atop the filament. These arcades seem to be consistently removed from the filament top. This allows a larger part of the filament to be exposed. Before the eruption, the filament becomes thicker, darker and more bulging than before, as seen from both the 304 and 171 Å images. Brightening of loops atop the filament can be seen for several times from the 171 and 94 Å passbands, indicating reconnections on-going there. The post-flare loops of the C3 flare are representative of these loops. Later, we will discuss the possible role of

this C3 flare and following reconnections in triggering the subsequent major eruption.

### 3. Correlation of the photospheric transverse field and the penumbral decay

In Figure 3 we present the long-term temporal evolution of 6173 Å intensity map (upper panels) and the photospheric transverse field ( $B_h$ , lower panels) of the AR derived from the HMI data.  $B_h$  is illustrated using a color map with red color representing stronger and blue representing weaker magnetic field strength.

This figure and the accompanying animation exhibit a very striking feature, that is the close correlation between the gradual changes of  $B_h$  and the WL intensity ( $I_c$ ). This feature is the focus of our study. Note that for completeness the data pre- and during the previous X2.1 flare have been included in the animation. Here we only focus on the data since 00:00 UT of September 7.

Initially, we see that the region with enhanced  $B_h$  is allocated with the PIL. Then, the red color of this region gradually evolves into a region of yellow, green and blue colors. This indicates that  $B_h$  there becomes weaker with time. After the peaking of the X1.8 flare, the  $B_h$  gets enhanced suddenly. On the other hand, the sunspot penumbrae around the PIL get brightened persistently in almost the same period ( $>10$  hours before the X1.8 flare), and become darkened suddenly during the flare. The changes of  $B_h$  and the penumbral structures during the flare are consistent with previous studies mentioned in our introduction. Of particular interest here is their long-term pre-flare evolution and correlation of the two quantities. In the earlier papers reported the flare-induced penumbra intensity changes (Wang et al. 2004; Deng et al., 2005), the authors adopted the wording “penumbral decay” to describe the process. Here we follow them on the terminology, although the wording “penumbral fade” might be a better choice since during

the process only the penumbral intensity changes considerably while the area remains largely unchanged.

To further examine their evolution and correlation, we select a trapezoid to include the main area of the pre-flare enhanced  $B_h$  region, which is around the PIL across the  $\delta$  spot. We then calculate the averages of the magnetic field components ( $B_h$  and  $B_z$ ), inclination angle ( $\theta_B$ ), total magnetic flux ( $\phi$ ), and the WL intensity ( $I_c$ ) within the trapezoid. The obtained profiles are plotted in the two panels of Figure 4. In the upper panel, we see that after  $\sim 7:00$  UT,  $B_h$  starts to decline gradually till the X1.8 flare, from an initial magnitude of  $\sim 1226$  G to a final value of  $\sim 679$  G. The overall declining percentage is  $\sim 45\%$ . During the X1.8 flare,  $B_h$  jumps to  $\sim 1053$  G. Similarly,  $\theta_B$  decreases from  $\sim 68^\circ$  (10:00 UT) to  $\sim 55^\circ$  before the flare, and jumps back to  $64^\circ$  after the flare (24:00 UT). On the other hand, the average intensity starts to increase also from  $\sim 10:00$  UT, from a normalized value of  $\sim 0.70$  to  $\sim 0.89$  before the flare and drops to 0.78 after the flare (24:00 UT). The intimate anti-correlation between  $I_c$  and  $B_h$  (or  $\theta_B$ ) is self-evident.

In the lower panel of Figure 4, we plot the profiles of the average positive and negative components of  $B_z$  as well as the total flux ( $\Phi$ ). We see that during the whole pre-flare stage, all the three quantities do not show any considerable systematic changes. The value of the positive (negative)  $B_z$  lies in a narrow range of [251, 280] G ( [-174, -215] G), and  $\Phi$  lies in a range of  $[0.58 \times 10^{18}, 0.65 \times 10^{18}]$  Maxwell, from 05:00 UT to 21:00 UT. This indicates that the PIL region is dominated by the transverse component of the photospheric field, and there is no significant flux emergence or cancellation in the period of study.

A straightforward explanation of the results shown in Figures 3 and 4 is that the magnetic field lines on the photosphere becomes more vertical with time during the pre-flare phase. To find further observational support of this explanation, we examine the AIA data taken in the 304 and 171 Å passbands. Following Ruan et al. (2014), we plot the

height-time map along a slice of the filament. The slice location and the map are shown in the upper panels of Figure 5, with an accompanying animation available online. A dashed white line is plotted for visual guide. We see that, along the slice, at about 08:00 UT the filament becomes thick enough to be observable from the map. After that, it shows a gradual ascending motion, very similar to the filament motion leading to the previous X2.1 flare (Ruan et al., 2014).

The 171 Å data present the filament and its overlying arcades. As described in the previous section, initially the filament seems to be buried underneath these arcades. Along with the continuous apparent expansion of the arcades, a larger part of the filament comes into view. To show this continuous expansion, we make an angular time map along a circular slice centered around one foot of the arcades. The northward direction is taken to be 0 degree and the angle increases clockwise. The slice and the map are shown in the lower panels of Figure 5, where the expansion is manifested as a gradual rotating motion, which is obvious from 05:00 UT on. The apparent expansion is initially very fast, then gets slower with time. The outer edge of the loops move from  $\sim 50^\circ$  at 05:00 UT to  $\sim 100^\circ$  at 12:00 UT and reaches  $\sim 120^\circ$  from 12:00 UT to 22:00 UT, along the circular slice. Note that thermal effects, which can make the coronal arcades visible or invisible, can result in some pseudo expansion. Nevertheless, with a careful inspection of the animation, we believe that the genuine physical expansion of the arcades is important here.

Assuming the pre-eruption corona field evolves slowly enough so that it can be represented by a series of magnetic equilibria, Liu et al. (2014) deduced this slow evolution with a Nonlinear Force-Free Field (NLFFF) extrapolation technique (Wieglemann, 2004; Wieglemann et al., 2006). In their Figure 4 and the accompanying animation, they showed the long-term evolution of the extrapolated electric current density distribution and magnetic field lines across the central part of the filament. It is clear from their study that

there exists a flux rope aligning with the filament and the flux rope arises gradually during the period from after the X2.1 to before the X1.8 flare. This result is consistent with the observation that a significant part of the well-developed filament exists after the X2.1 flare (see also Liu et al. 2014), and supports our argument deduced above.

In summary, we found a persistent well-correlated pre-flare long term evolution of the penumbral structure and the photospheric transverse field around the PIL. The observed penumbral decay and  $B_h$  decline are likely caused by the ascending motion of the filament-flux rope system. This picture is supported by the simultaneous imaging data with the 304 Å for the filament and the 171 Å for the overlying arcades. Nevertheless, it cannot be ruled out of the possibility that the pre-flare sunspot decay and the  $B_h$  decline are simply the result of the overall sunspot evolution and not the direct response to the filament-corona dynamics.

#### 4. Possible triggering process of the major eruption

Another interesting problem to discuss here is the possible role played by the C3 flare in triggering the following X1.8 eruption. To show this, in Figure 6 we present the four AIA 171 Å images from 20:39 UT to 22:27 UT. The first panel presents the post loops of the C3 flare, stretching over the filament. A nearby bright loop on the northern side is also shown. In the second panel both loops get darkened and expanded. In the third panel (21:54 UT) a new loop connecting the southern foot of the post-flare loops and the eastern foot of the nearby loop appears. This is very likely a result of the reconnection between the two loop systems, as will be explained in the following paragraph. At 22:27 UT, in the fourth panel, the post-reconnection loops get brightened considerably and the post-C3 loops almost disappear. This evolution of coronal loops can also be clearly seen from the accompanying AIA 171 Å animation.

To support this reconnection scenario, we show the contours of the vertical magnetic field component of HMI in Figure 6 (b). It is seen that the magnetic field polarities are in the order of positive, negative, positive, and negative for the four foots of the two sets of pre-reconnection loops, thus favoring the reconnection process described above. The post-reconnection bright loops (see Figure 6d) are still likely on top of the filament and more high-lying in the corona in comparison to those pre-reconnection overlying loops. Shortly after the reconnection, the filament starts to rise rapidly and the X1.8 flare takes place.

To illustrate the reconnection process more clearly, we show schematics in the left two panels at the bottom of Figure 6, where yellow lines are for pre-reconnection loops and red lines are for post-reconnection loops. It can be seen that the expansion of the coronal arcades overlying the filament (in cyan) drives their reconnection with longer magnetic loops rooted in a nearby pair of opposite polarities. This reconnection can remove some of the arcades overlying the filament and reduce the confining force (or the strapping effect, see recent paper of Wang et al., 2015) acting on the filament. This will at least speed up the evolution process leading to the following major eruption, and possibly play as a trigger of the filament-flux rope instability. **Possible configuration during the impulsive stage of the X1.8 flare is also shown in the last panel of Figure 6, for completeness, from which we see that the filament erupts with a flux rope and part of its overlying arcades.** The picture involves a quadrupolar topology and a triggering reconnection in the corona, both are essential features of the breakout model (Antiochos et al., 1999) for solar eruption. We therefore suggest that the breakout process may be important to the trigger of the X1.8 flare and the associated CME.

## 5. Conclusions and discussion

Some recent studies on the magnetic field evolution have been focusing on rapid changes of the photospheric transverse field and sunspot structures induced by solar flares. In this study we investigate the correlation between the long-term ( $\sim 10$ -20 hours) pre-flare evolution of the sunspot penumbrae and the photospheric transverse field component around the PIL, as well as their relation with filament-corona dynamics. It is found that the penumbrae decayed gradually and the strength of the transverse field (and the inclination angle of the magnetic field) on the solar surface declined correspondingly, indicating that the pre-flare magnetic structure from the photosphere to the corona is getting more vertical with time. This indication is corroborated with the SDO imaging observation of the filament arising and the apparent expansion of its overlying arcades, and consistent with the NLFFF extrapolation results of the pre-eruption state of the local corona.

Intensity changes of the sunspot penumbra induced by solar flares have been reported in several studies (e.g., Wang et al., 2004; Deng et al., 2005; Liu et al., 2014). Here we report the long-term pre-flare evolution of the penumbra intensity change as well as its correlation with the photospheric magnetic field evolution and relevant coronal dynamics. In Deng et al. (2005), the flare-induced penumbra decay was explained with the change of the inclination angle of the magnetic field in the corresponding penumbral region. According to Leka & Skumanich (1998), the magnetic field inclination angle in the peripheral penumbrae, when turning from more inclined to more vertical and toward the umbra, can directly suppress the penumbral Evershed flow resulting in an increase of the continuum intensity. Here we propose a very similar scenario to interpret the observational result, although the trend of long term change is opposite to that of the flare-induced rapid changes. We suggest that the observed persistent pre-flare penumbral decay (or fade) is a result of the gradual change of the direction of the magnetic field in the penumbral region from more

horizontal to more vertical, which is likely caused by the gradual rising of the filament-flux rope system in the upper solar atmosphere.

The long-term pre-flare behavior of the photospheric magnetic field, sunspot, filament and the corona arcades are of vital importance to space weather studies. These behaviors could provide clues about how the solar magnetic field evolves from a pre-eruption state to the eruption, including the energy transport, storage, and release processes. The result of our study is based on eruptions from only one AR. More events should be investigated to decide what signatures or processes could be used as possible eruption precursor or trigger.

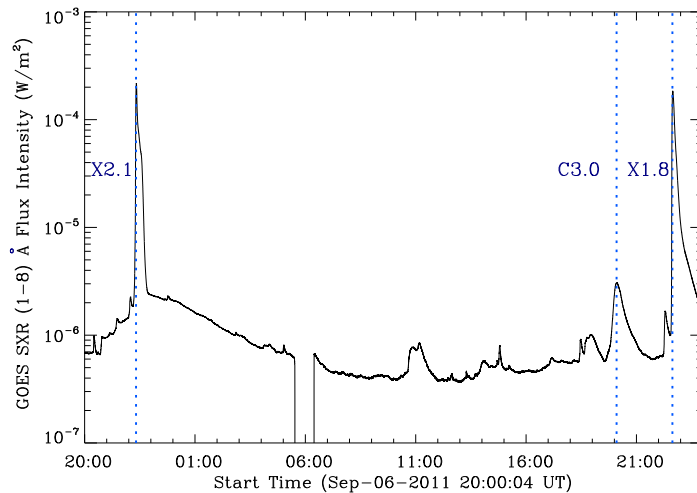


Fig. 1.— The 1-8 Å GOES SXR flux intensity profiles from 20:00 UT September 6 to 24:00 UT September 7. The peaking times of these three flares X2.1 (22:20 UT), C3.0 (20:06 UT), X1.8 (22:38 UT) have been labelled with blue vertical dotted lines. An animation and a color version of this figure are available online.

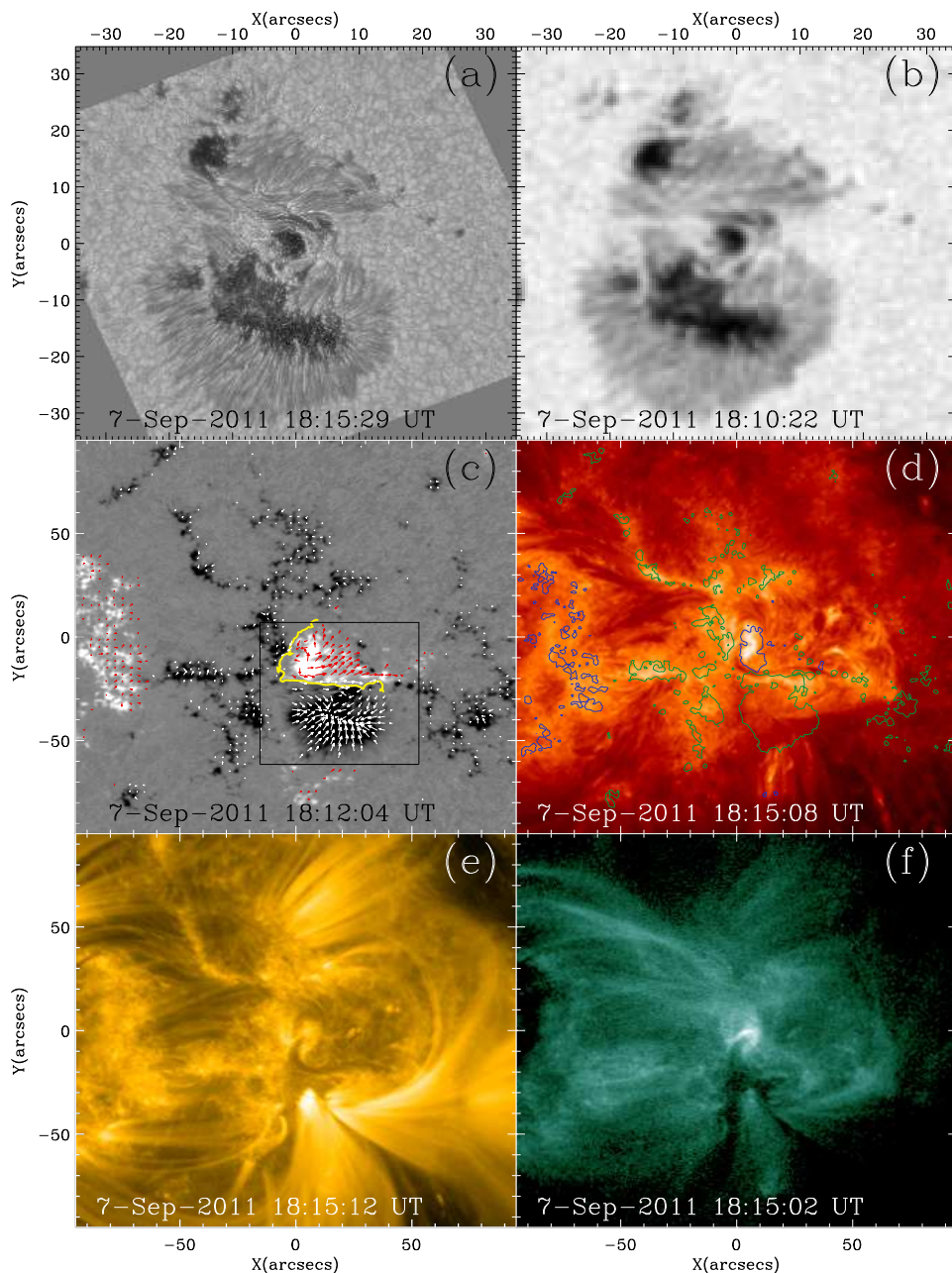


Fig. 2.— Pre-eruption observations of the AR 11283: (a) the BBSO high-resolution image taken at 18:15 UT, (b) the HMI 6173 Å intensity image, (c) the HMI vector magnetic field with the color map representing the vertical field component ( $B_z$ ) and arrows for the  $B_h$  component, (d) to (f) the 304, 171, and 94 Å images recorded by SDO. The contours in panel (d) are given by  $\pm 300$  G of the HMI vertical field component ( $B_z$ ) on the solar surface. The FOV of panels (a) and (b) has been marked in panel (c) with a square. A color version of this figure is available online.

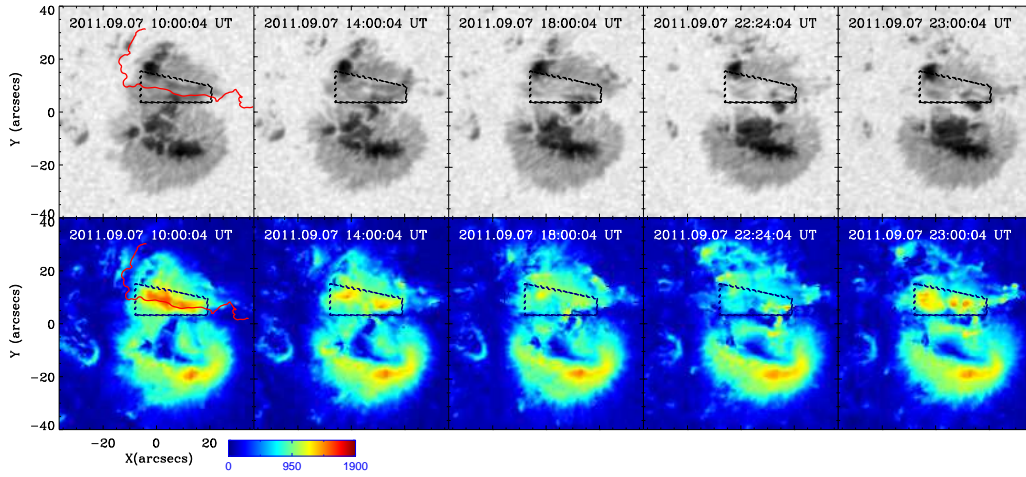


Fig. 3.— Temporal evolution of 6173 Å intensity map (upper panels) and the photospheric transverse field strength ( $B_h$ , lower panels) of the AR given by HMI. An animation and a color version of this figure are available online.

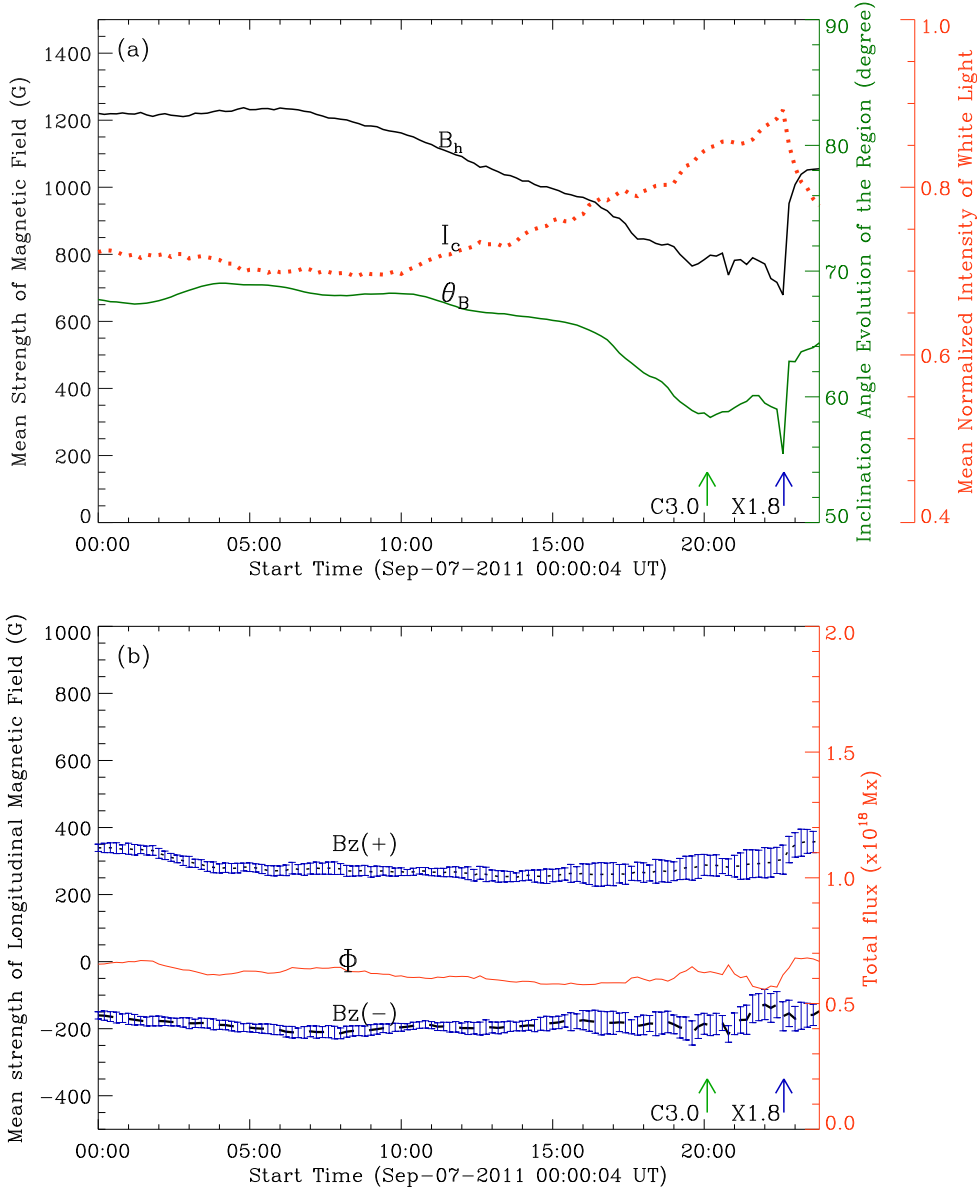


Fig. 4.— (a) Temporal profiles of the average transverse field strength  $B_h$ , average inclination angle  $\theta_B$  and normalized white-light intensity  $I_c$ , and (b) Temporal profiles of the average positive and negative components of  $B_z$  as well as the total flux ( $\Phi$ ). All parameters are calculated in the area defined by the trapezoid shown in Figure 3. A color version of this figure is available online.

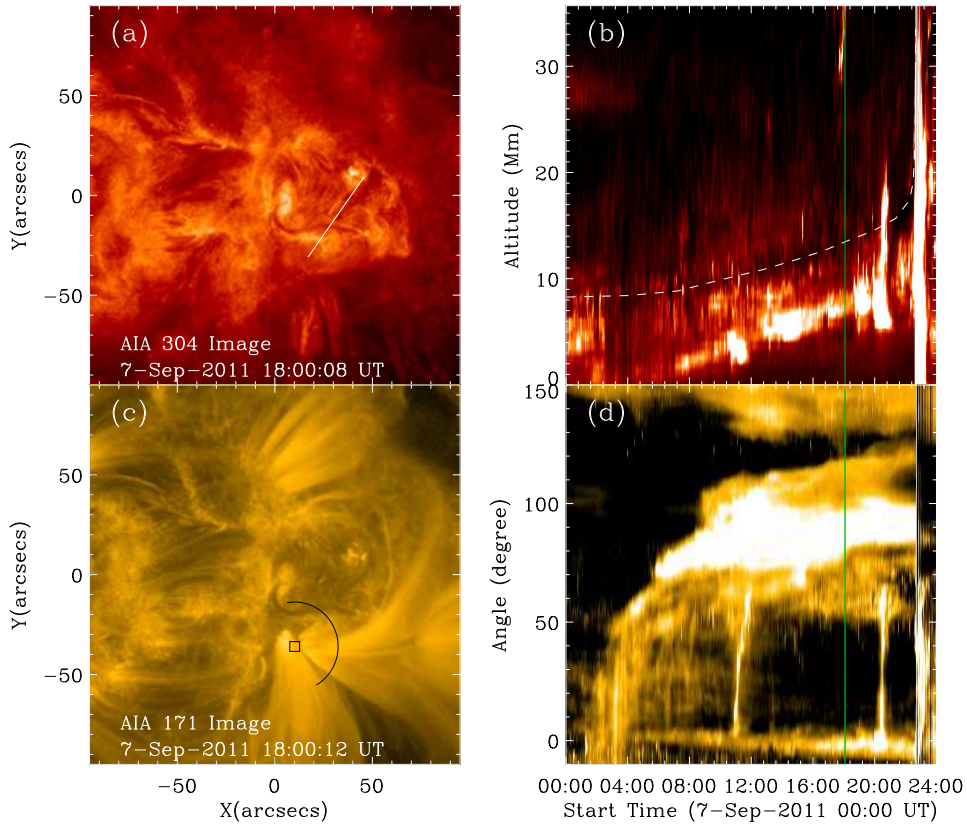


Fig. 5.— Time-stacked images along specified slices of the filament and the overlying arcades. Panels (a) and (c) show the direct images of AIA/SDO at 18:00 UT on September 7, 2011 in the 304 Å and 171 Å passbands, with the location of the slices. The green vertical lines in (b) and (d) represent the observation times of panels (a) and (c). An animation and a color version of this figure are available online.

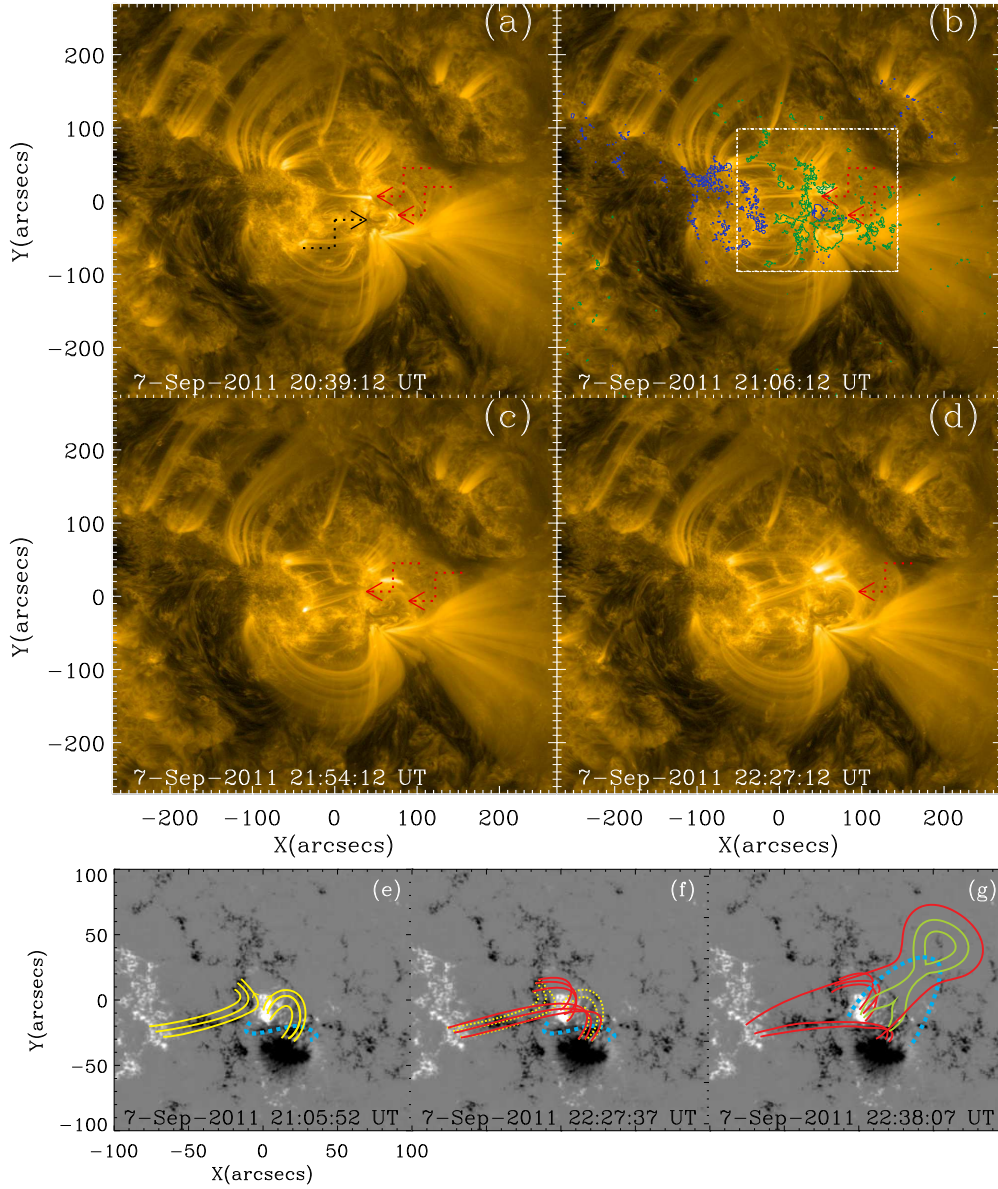


Fig. 6.— Panels (a-d): The AIA 171 Å images from 20:39 UT to 22:27 UT. The contours in panel (b) are given by 300 G for the positive component (in blue) and 200 G for the negative component (in green) of  $B_z$  on the solar surface. Red arrows point to the loops of interest, and the black arrow in panel (a) points to the filament of study. Panels (e-g): Schematics showing the proposed reconnection-triggering process **and possible magnetic configuration during the impulsive stage of the major eruption**. The pre-reconnection magnetic field lines are in yellow and post-reconnection lines are in red, and the filament of study is depicted with a cyan dashed line. Arrows in (e) indicate the magnetic field direction. An animation and a color version of this figure are available online.

We thank SDO/HMI and SDO/AIA science teams for the free access to the data. We are grateful to the referee for valuable comments and Dr. Guohui Du, Bing Wang, and Di Zhao for their help in preparing the figures. This work was supported by the 973 program NSBRSF 2012CB825601, U1331104 and NNSFC grants 41331068, 41274175 to SDUWH, and by NSF grants AGS-1348513 and AGS-1408703 to NJIT.

## REFERENCES

- Antiochos, S. K., DeVore, C. R., Klimchuk, J. A., 1999, *ApJ*, 510, 485
- Brueckner, G. E., Howard, R. A., Koomen, M. J., et al. 1995, *SoPh*, 162, 357
- Cao, W., Gorceix, N., Coulter, R., Ahn, K., Rimmele, T. R., & Goode, P. R. 2010, *Astronomische Nachrichten*, 331, 636
- Deng, N., Liu, C., Yang, G. et al., 2005, *ApJ*, 623, 1195
- Evershed J., 1909, *Mon. Not. R. Astron. Soc.* 69, 454.
- Feng, L., Wiegmann, T., Su, Y., et al. 2013, *ApJ*, 765, 37
- Goode, P. R., Yurchyshyn, V., Cao, W., Abramenko, V., Andic, A., Ahn, K., & Chae, J. 2010, *ApJ*, 714, L31
- Hudson, H. S., 2000, *ApJ*, 531, L75
- Jiang, C. W., & Feng, X. S. 2013, *ApJ*, 769, 144
- Lemen, J. R., Title, A. M., Akin, D. J., Boerner, P. F., & et al. 2012, *Solar Phys.*, 275, 17
- Leka, K. D., & Skumanich, A. 1998, *ApJ*, 507, 454
- Lin, J., Soon, W., & Baliunas, S. L. 2003, *New Astron. Rev.*, 47, 53
- Liu, C., Deng, N., Lee, J. et al., 2014, *ApJ*, 795, 128
- McKenzie, D.E. and Hudson, H.S.: 1999, *Astrophys. J.* 519, L93
- Moore, R. L., Sterling, A. C., Hudson, H. S., & Lemen, J. R. 2001, *ApJ*, 552, 833
- Pesnell, W. Dean, Thompson, B. J., Chamberlin, P. C., 2012, *Solar Phys.*, 275, 3

- Ruan, G.P., Chen, Y., Wang, S., Zhang, H.Q., Li, G., Jing, J., Su, J.T., Li, X., Xu, H.Q.,  
Du, G.H., & Wang, H.M., 2014, *ApJ*, 784, 165.
- Rust, D. M., & Kumar, A. 1994, *Sol. Phys.*, 155, 69
- Schou, J., Scherrer, P. H., Bush, R. I., Wachter, R., et al. 2012, *Solar Phys.*, 275, 229
- Severny, A. B., 1964, *ARA&A*, 2, 363
- Shen, Y.D., Ichimoto, K., Ishii, T. T., Tian, Z.J., Zhao, R.J., Shibata, K., 2014, *ApJ*, 786,  
151
- Spirock, T. J., Yurchyshyn, V., Wang, H., 2002, *ApJ*, 572, 1072
- Titov, V.S. and Demoulin, P.: 1999, *Astron. and Astrophys.* 351, 707
- Wang, H., Ewell, M. W., Zirin, H., Ai G., 1994, *ApJ*, 424, 436
- Wang, H., Liu, C., Qiu, J., Deng, N., Goode, P. R., & Denker, C. 2004, *ApJ*, 601, L195
- Wang, H. M., Liu, C. 2010, *ApJl*, 716, L195
- Wang, H. M., Cao, W. D., Liu, C., Xu, Y., Liu, R., Zeng, Z. C., Chae, J. C., Ji, H. S., 2015,  
*Nature communications*, DOI: 10.1038/ncomms8008
- Wang, S., Liu, C., Liu, R., Deng, N., Liu, Y., & Wang, H. M., 2012, *ApJ*, 745, L17
- Wiegmann, T. 2004, *Sol. Phys.*, 219, 87
- Wiegmann, T., Inhester, B., & Sakurai, T. 2006, *Sol. Phys.*, 233, 215
- Yurchyshyn, V., Wang, H., Abramenko, V. et al., 2004, *ApJ*, 605, 546
- Zharkov, S., Green, L. M., Matthews, S. A., & Zharkova, V. V. 2013, *JPhCS*, 440, 012046